



Patterned anodes with sub-millimeter spatial resolution for large-area MCP-based photodetector systems

Jinseo Park^{*}, Fangjian Wu, Evan Angelico, Henry J. Frisch, Eric Spieglan

Enrico Fermi Institute, The University of Chicago, United States of America

ARTICLE INFO

Keywords:

Microchannel-plate photomultipliers (MCP-PMT)
Large systems
Electronic channel count
Anode
Pattern
Capacitive coupling
Spatial resolution
Rate
Occupancy

ABSTRACT

Micro-channel-plate-based photo-detectors are unique in being capable of covering very large areas such as those required in elementary particle and nuclear physics, while providing sub-millimeter space resolution, time resolutions of less than 10 picoseconds for charged particles, and time resolutions of 30 psec–50 psec for single photons. In such systems the electronic channel count is a major cost driver. Incorporating a capacitively-coupled anode allows the use of external pickup electrodes with patterns of individual channels optimized for occupancy, rate, and time/space resolution. The signal pickup antenna can be economically implemented as a printed circuit card with a 2-dimensional array of pads for high-occupancy/high-rate applications such as in particle colliders and medical imaging, or a 1-dimensional array of strips for a lower channel count in low-occupancy/low-rate applications such as large neutrino detectors. Here we present pad patterns that enhance signal-sharing between pads to lower the channel count per unit area in large-area systems by factors up to 4, while maintaining spatial resolutions of approximately 100 to 200 μm for charged particles and 400 to 1000 μm for single photons. Patterns that use multiple signal layers in the signal-pickup board can lower the channel count even further, moving the scaling behavior in the number of pads versus total area from quadratic to linear.

1. Introduction

The development of large-area micro-channel-plate-based photodetectors (MCP-PMTs) such as the LAPPDTM [1,2] with sub-mm space resolution and time resolutions of < 10 psec for charged particles [2–5] and < 30–50 psec for single photons [6] enables 3-dimensional imaging of charged particle tracks in transparent media [7,8].

In particle and nuclear physics there are large experiments that require many square meters of photosensitive coverage. Examples include the current JUNO neutrino experiment with 20,000 50.8 cm-diameter phototubes [9], the 2009 commercial proposal for a 3-year production of 100,000 MCP-based LAPPDTM photodetectors for the proposed DUSEL neutrino detector [2], and the current Theia proposal employing 10,000 LAPPDs [10]. In medical imaging, a single low-dose whole body TOF-PET scanner based on LAPPDs would require 5m²–10 m² [11–14].

For such large detector systems and high-volume medical facilities, economies in the number of photodetectors required and the electronic channel count are essential. The photodetector count can be reduced by factors greater than two by reconstruction of reflected photons [7,8]. Here we address the reduction of the electronic channel count per individual photodetector by similar factors using enhanced charge sharing among anode readout pads.

The planar geometry of MCP-PMTs allows capacitive coupling of the signal induced on the anode plane to a plane of signal-pickup electrodes external to the detector vacuum package. This has been extensively explored using a dielectric anode substrate [15–23]. The recently-developed fast rise times and higher gains inherent in ALD-coated MCP-PMT signals [1,24–28] alternatively allow the use of a metal internal anode, with the resistance of the thin metal layer acting as a high-pass RC filter for signals transmitted through the metal layer and the vacuum package base [29]. The external signal-pickup geometry, which is the focus of this paper, can be implemented as printed circuit boards, a widely-available and economical technology.

The geometry of anode readout patterns has also been well-explored in the context of other large-area technologies [30,31]. Here we focus on MCP-PMT anode patterns for the charge clouds produced by single photons and by charged particles traversing the photodetector entrance window.

The organization of the paper is as follows. Section 2 discusses the shape of the image of the charge produced by single photons and Cherenkov emission in the entrance window. The calculation of spatial resolution is presented in Section 3 as a function of the ratio of pad pitch to charge cloud diameter. Results from the simulation of a high-sharing pattern are compared to those from a pattern of square

^{*} Corresponding author.

E-mail address: truewis@uchicago.edu (J. Park).

pads in Section 4. Section 5 introduces a method for lower-occupancy applications that uses connections on multiple layers of the signal pickup board to change the scaling behavior of channel count versus area from quadratic to linear. The details of the discrete simulation used in calculating charge sharing among pads are presented in [Appendix](#).

2. The image of the charge distribution from signals in MCP-based photomultipliers

Signals induced on a segmented anode, or equivalently a capacitively coupled signal pickup board [29], can be analyzed to constrain the position of the incident particle. Here we consider the case of an array of pads with a regular pitch. Knowledge of the image shape at the anode plane and modeling of the sharing between pads yield a measurement of the position of the image at much higher resolution than the pad size.

We consider two cases, the image generated by a single photon incident on the photocathode, leading to an MCP cascade initiated by a single photoelectron (Section 2.1); and the image generated by a charged particle producing Cherenkov light in the photodetector entrance window, generating many photoelectrons distributed into multiple MCP pores (Section 2.2) [32,33].

2.1. The image from a single photoelectron

The amplification of a photoelectron in a chevron stack of ALD-functionalized micro-channel plates produces a cloud of $\geq 10^7$ electrons above the anode plane. As the charge cloud drifts to the anode, image currents are induced in response to the changing electro-magnetic field lines at the anode surface.

The spatial dimensions of the charge-cloud image are largely set by the spatial dimensions of the charge avalanche [34]. Among the factors playing a role in determining the transverse dimensions of the signals induced in the anode are: (1) the initial image of photons on the photocathode; (2) the length of the gap and voltage between the two MCPs in the chevron; (3) the length of the gap and voltage between the exit MCP and the anode; (4) the end-spoiling, bias angle, and secondary-emitting layers of the MCP pores [35]; and (5) the geometry of the pickup pattern. In the case of a capacitively coupled anode, the resistance of the internal anode layer as well as its separation from the pickup plane will also affect the size of the image.

Measurements of the anode image radius from a single photoelectron depend on both the detector geometry and the configuration of the measurement [34,36]. Signal distributions are typically fit to a Gaussian in either voltage or time-integrated voltage with the standard deviation representing the transverse size. Measured image sizes vary from 0.5 mm to 5 mm radius [34,36]. The radii in these measurements have been found to be most strongly dependent on the separation distances of the active layers in the MCP-PMT and the applied voltages that accelerate the electron cloud [34].

2.2. The image from a charged particle that produces Cherenkov light in the photocathode window

Charged particles may be detected by MCP-PMTs using Cherenkov light produced in the transparent entrance window [32]. The arrival of Cherenkov photons is a good proxy for the arrival-time of charged particles as Cherenkov emission preserves timing at the sub-picosecond level [37]. After traveling through the window at the (wave-length dependent) Cherenkov-emission angle, photons originating on the particle trajectory are converted to photoelectrons by the photocathode. The photoelectrons are then proximity-focused to the pores of the MCP where they interact to initiate amplification. Here we assume normal incidence of the charged particle; off-angle incidence will produce measurable, and hence exploitable, effects depending on the anode pattern, but is beyond the scope of this paper.

Cherenkov photons are emitted in the window at an angle θ_c such that $\cos \theta_c = 1/\beta n(\lambda)$ [37]. Charged particles at normal incidence produce a circular spot centered on the transverse position of the particle with a maximum radius $T \tan \theta_c$, where T is the thickness of the window or radiator. For Schott B33 glass [38,39], a typical material for photo-detector windows, the Cherenkov angle ranges from $\theta_c = 48.3^\circ$ at 300 nm to 47.1° at 700 nm. The resulting Cherenkov photon-spot radius is roughly equal to the thickness of the radiator. Using the typical performance of bi-alkali photocathodes and the transmission of B33 glass windows, the number of photoelectrons is ≈ 66 per centimeter; for fused silica, the number of photoelectrons increases to ≈ 200 per centimeter due to enhanced ultra-violet transmission [33].

For an internal (as opposed to capacitively coupled) anode consisting of a 1-dimensional array of strip-line conductors with 5.1 mm width and 6.9 mm pitch, and a window with 5 mm thickness, the measured transverse size of the charged-particle signal is (10 ± 2.5) mm FWHM¹ [33]. The FWHM was determined by fitting the signal shape with a Gaussian distribution.

In this paper the shape of a charged-particle signal is modeled as a bivariate Gaussian. A small Monte Carlo simulation was made that (1) generates 30 Cherenkov photon positions and angles in a 5 mm window, (2) generates photoelectron positions corresponding to the incident position of the Cherenkov photons, and (3) sums the resulting signal image distributions assuming that the single photoelectron distribution is a bivariate Gaussian with a 5 mm standard deviation. The resulting signal-image shape from 5000 events is a bivariate signal distribution with kurtosis of 2.85 ± 0.12 , where a Gaussian kurtosis corresponds to a value of 3.

3. Sub-millimeter position reconstruction using patterned anodes

Capacitive coupling of the anode plane enables the use of printed circuit boards as the external signal-pickup component [29]. These may be designed in complex patterns optimized for specific applications using widely-available computer programs. Because the pickup boards are external to and electrically isolated from the photomultiplier, they can be replaced without changes to the detector module. Printed circuit boards are inexpensive and widely available with fast turnaround which enables rapid optimization.

Spatial resolutions of $\approx 300 \mu\text{m}$ have been obtained using a signal-pickup board with 12.7 mm-square pads for signal-source locations for which there is charge sharing between neighboring pads [29]. However when the image of the charge cloud is fully contained within one pad, the resolution becomes substantially worse depending on the ratio of the pad size to the diameter of the image.

Large-area, high-rate applications such as high-energy particle colliders and some medical applications are natural candidates for pad-based signal pickup segmentation. However, the number of channels grows quadratically with inverse pad size. Section 4 compares results from simulations of the spatial resolution using signal sharing for two segmented anode patterns: a square pad pattern and a sinusoidal pad pattern with enhanced sharing.

3.1. Calculation of spatial resolution

The uncertainty on the incident photon or particle position is a function of the position in the pad array due to the position dependence of the overlap with neighboring pads. To calculate the resolution, an initial estimate of the position is the center of the pad with the strongest signal. The resolution is then calculated from signal distributions for the pad and its neighbors by simulating particles hitting different positions

¹ This measurement was made with an LAPPDTM with two 1.3 mm MCPs separated by approximately 2 mm and a distance of about 6 mm between the exit MCP and anode. The MCPs were each biased at 900 V, photocathode at 20 V, and 200 V across each of the gaps.

on and around the pad, using a constant total signal at the anode, but with varying distributions on the pads depending on position. In the simulation we use the values of the electronic noise measured for the PSEC4 waveform sampling system [8,33,40], which is the limiting factor on the resolution in the presence of charge sharing.

To simulate and calculate the local spatial resolution for many discrete points on a segmented pattern, the signal collected by each pad is calculated using the overlap of the image distribution, modeled as a bivariate Gaussian, with each pad. The collection of all simulated positions forms a look-up table of signals on the pads versus particle hit position. From the look-up table, a 2D signal gradient, is calculated as a function of the charge-image position. The derivation of this function is described in [Appendix](#).

3.2. The effect of electronic noise on reconstruction using pad sharing

The determination of the image position using the relative sharing between pads has inherent uncertainties due to electronic noise as well as possible fluctuations and non-uniformities in the MCP amplification stages. These sources of noise increase the degree of signal-sharing required for a desired spatial resolution.

The voltage noise of modern-day, fast-sampling waveform digitizers used to measure MCP-PMT signals is on the order of 0.5 mV–1 mV. For example, the PSEC4 digitizing ASIC for digitizing LAPPDs has an RMS voltage noise of about 700 μ V [8,40].

The signal amplitudes from single photoelectrons detected by MCP-PMTs are determined by the gain of the detector, the capacitance and impedance properties of the anode, the size and shape of the anode pads, and the size and shape of the charge-cloud image. MCP-PMTs are current sources; a gain of 10^7 and a pulse width of 1 nsec corresponds to a current of 1.6 mA, which into 50 Ω produces an 80 mV peak voltage. A higher gain, such is typical of ALD-coated MCPs operated with a larger voltage across the photocathode-MCP gap [28], a shorter pulse such as with MCPs with 10-micron pores, or a higher input impedance would give proportionally larger pulses. However, for a capacitively coupled anode there is a reduction in amplitude due to attenuation through the coupling to the signal pickup board and the sharing among pads on the pickup pattern [29].

For an LAPPD with an internal strip-line anode, the noise of the PSEC4 electronics increases from 700 μ V to about 1.5 mV due to the antenna-like properties of the cables and strip lines [33]. At a gain of 3×10^7 , an LAPPD with the same strip-line anode pattern measured a single photoelectron pulse-amplitude distribution with a peak at 60 mV [6].

Because the noise-to-signal ratio varies depending on detector settings and anode configuration, we choose a conservative ratio of 7.5% which takes into account the measured 1.5 mV noise and a detector with a (modest) gain of 10^7 , resulting in 20 mV single photoelectron amplitude. This is the noise value σ_C used in the simulation of single photoelectrons in the results to follow, which enter in the resolution calculation detailed in [Appendix](#).

A charged particle passing through the window will typically produce many tens of photoelectrons, increasing the signal amplitude to greater than 100 mV. At the limit of high signal amplitude, the limiting factor in reconstructing the position of the charged particle using the method of sharing will be the modeling of the transverse shape and distribution of the image. In the results to follow, resolution functions corresponding to a 1% noise-to-signal ratio are plotted alongside the single photoelectron case.

The resulting resolution functions scale linearly with the noise-to-signal ratio. The noise levels used here, though based on observations from experimental setups, are somewhat arbitrary due to the dependence on detector settings. The resulting resolutions can be scaled to correspond to a particular experimental setup.

4. Anode pattern simulation results

We apply the algorithm of [Appendix](#) to two patterns: a regular pattern of square pads and a pattern of sinusoidal pads which has reduced channel count per unit area and enhanced signal sharing. To allow the results to be used independent of the details of the image formation (Section 2.2), for a given pattern the spatial resolutions are calculated as a function of the size of the pads via a scale factor, L , defined as the ratio of the pad-to-pad pitch to the diameter of the image of the charge cloud. As an example, $L = 2$ corresponds to half as many pads per unit length compared to $L = 1$, and one quarter as many per unit area.

The diameter of the image, modeled as a bivariate Gaussian, is defined as the size at 4 standard deviations (4σ). To relate to previous measurements, and to have a spatial scale for comparison, the bivariate Gaussian standard deviation is set to 4.2 mm which corresponds to the 10 mm FWHM measured in [33] and described in Section 2.2.

4.1. Square and sinusoidal pads

A 3×3 portion of a square-pad pattern, such as used in the measurements of [29], is shown in the left-hand panel of [Fig. 1](#). The black circle outlines the 2σ boundary of an example of a simulated bivariate Gaussian representing the charge image from a single photoelectron or charged particle. In this figure, the ratio of the pitch to the diameter of the charge image, the scale factor L , is 1.0.

One motivating design principle in increasing the degree of signal sharing between pads is to distort the boundaries of the square pads such that the image can never fit entirely within one pad. An example is the sinusoidal-pad pattern shown on the right-hand panel of [Fig. 1](#). This pattern has the same pad pitch and introduces an additional parameter: the amplitude of the sine-wave distortion. The amplitude shown in the figure is half of the pitch.

4.2. Response of neighboring cells versus incident position

The fraction of the total signal measured on each of two neighboring cells is shown in [Fig. 2](#) as the image position is scanned across the line $y = 0$. The signal on each pad follows the fractional overlap of the image with the each pad. Electronic noise with magnitude 7.5% of the injected signal intensity is included on each channel, providing a limit to the ratio between pads. The right-hand plot demonstrates the larger degree of signal sharing on the sinusoidal pattern.

The ratio of the injected signal on each of two neighboring cells as the image position is scanned across the line $y = 0$ is shown in [Fig. 3](#) for both the square (Left) and sinusoidal (Right) patterns.

4.3. Position resolution versus incident particle position

The local spatial resolution at each position on a segmented anode may be calculated as a function of the incident signal position for the entire pattern using the methodology outlined in [Appendix](#). The resulting spatial resolutions of the square and sinusoidal patterns are presented in this section for a noise-to-signal-intensity ratio of 7.5% (single photoelectrons) and 1% (charged particles).

All spatial resolutions are reported in microns, but are directly proportional to the noise-to-signal-intensity ratio. For example, a resolution of 100 μ m shown here in the case of 1% noise would represent a resolution of 1000 μ m in the case of 10% noise.

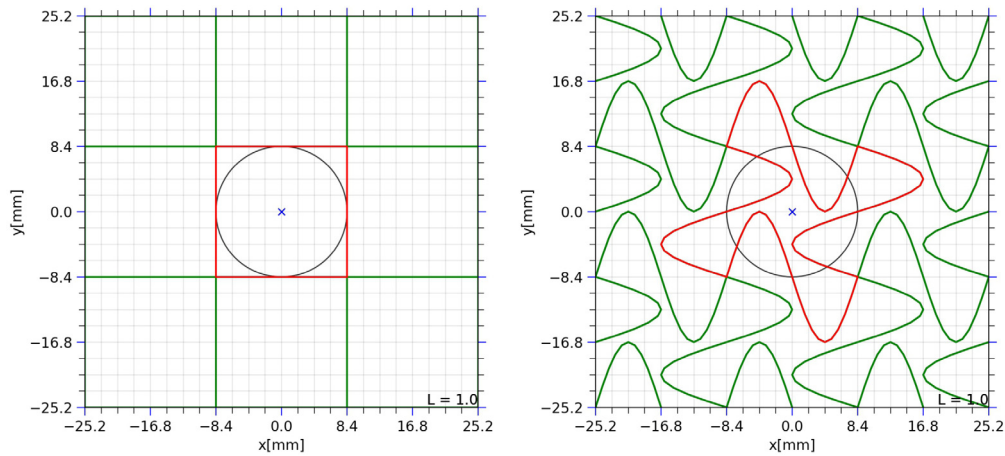


Fig. 1. Left: Nine cells of a square-pad pattern. The black circle outlines the 2σ boundary of an example of a simulated bivariate Gaussian. Right: The sinusoidal-pad pattern. The amplitude of the sine wave is the half of the pad pitch. The central pad in both patterns is outlined in red for visual clarity. (For interpretation of the references to color in this figure legend, the reader is referred to the web version of this article.)

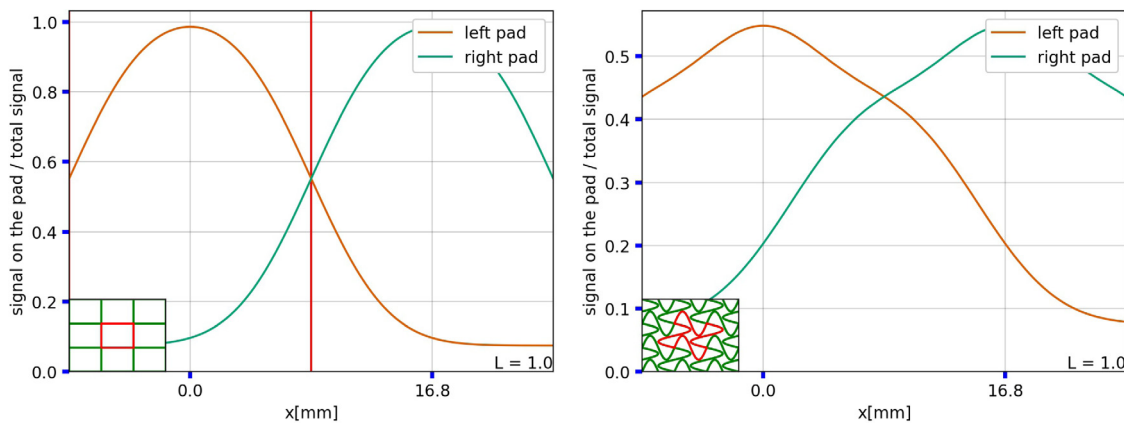


Fig. 2. The fractional signal intensity of two adjacent pads as the horizontal position of the image is scanned over the pads. Left: Square pad pattern. Right: Sinusoidal pad pattern.

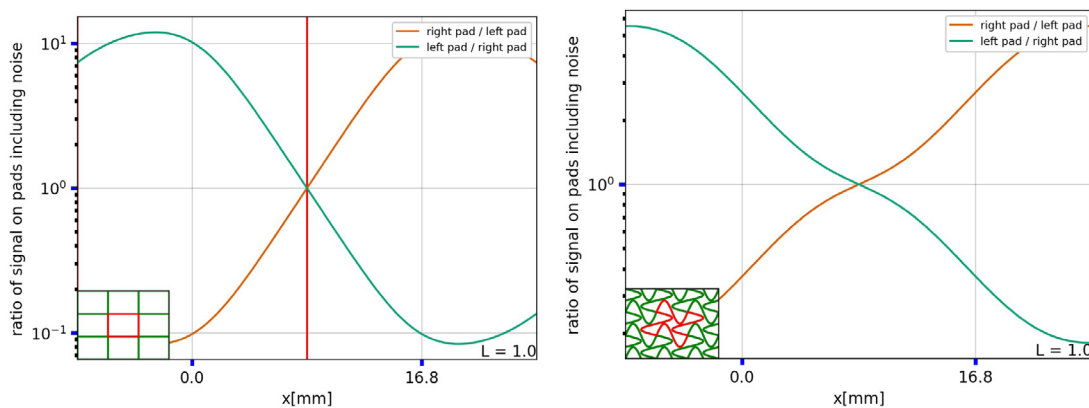


Fig. 3. The signal ratio of neighboring pads as the horizontal position of the image is scanned across the line $y = 0$. Left: Square pad pattern. Right: Sinusoidal pad pattern.

4.3.1. Resolution functions in 2D for fixed scale factor L

The 2D resolution functions for the square and sinusoidal patterns are shown in Fig. 4. The resolution is calculated using the signal-gradient method of Appendix with 7.5% noise σ_C . Locations where the resolution function has local maxima represent locations where the gradient of the signal distribution is smallest. These local maxima may be used to inform further optimization of the pattern design. The best local position uncertainty for the square pattern is ≈ 550 microns,

with a worst-case local position uncertainty of ≈ 770 microns when the image is centered on the pad.

A one dimensional slice of the 2D resolution function along the line $y = 0$ is shown in Fig. 5. In the following section, the 10th and 90th percentile, as well as the median, of the full 2D resolution functions are reported as a metric of pattern performance.

4.3.2. Resolution as a function of the pad size

The scale factor L determines the number of pads and hence the channel count per unit area. A scale factor of $L = 1.0$ corresponds to no

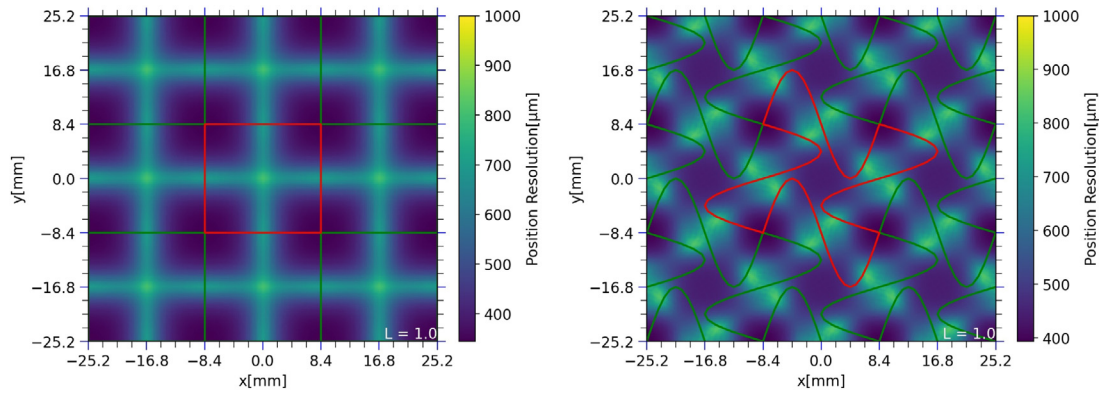


Fig. 4. The position resolution as a function of incident position for a noise-to-signal ratio of 7.5%. Left: Square pad pattern. Right: Sinusoidal pad pattern.

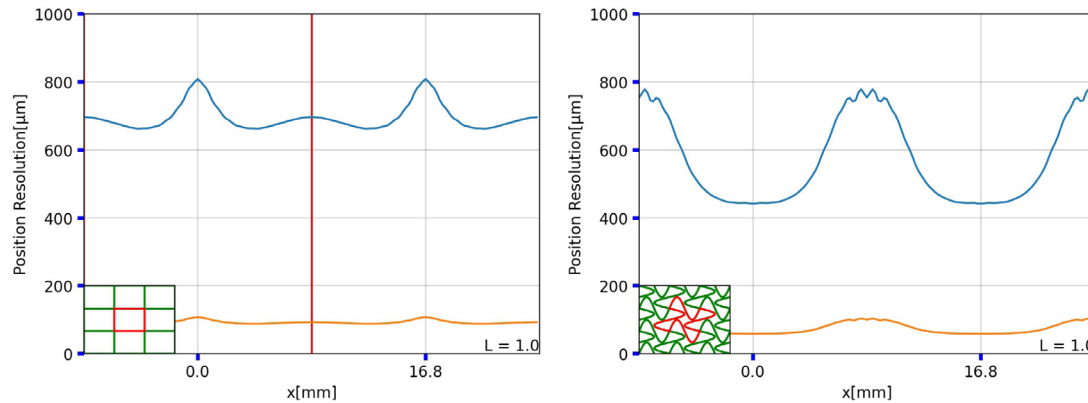


Fig. 5. A slice of the position resolution functional at $y = 0$. The blue lines represent a noise level of 7.5% and the orange lines represent a noise level of 1%. Left: Square pad pattern. Right: Sinusoidal pad pattern. The ripples on the peaks of the sinusoidal pattern's function are generated by the discretization of the anode, look-up table, and signal shape function. (For interpretation of the references to color in this figure legend, the reader is referred to the web version of this article.)

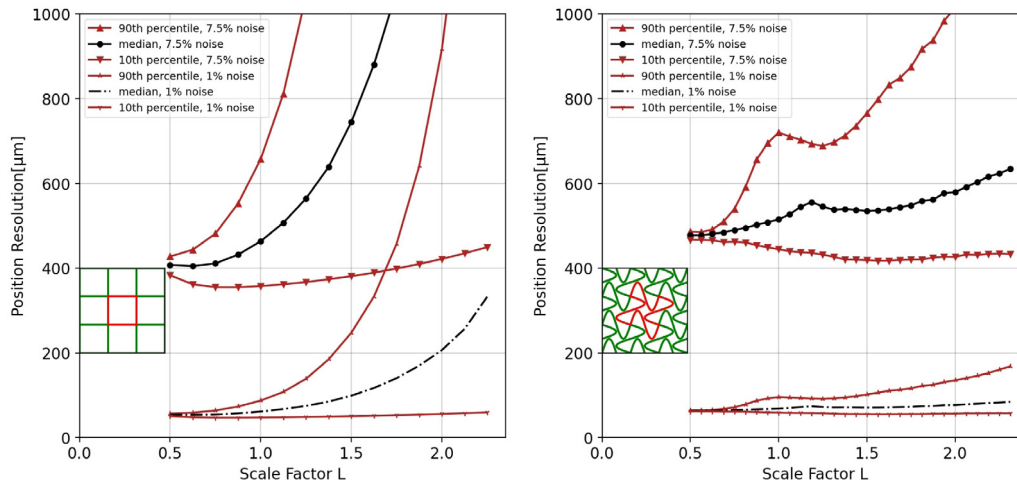


Fig. 6. The median, 10th, and 90th percentile of the 2D position resolution as a function of the scale factor L . The top set of curves have a noise level of 7.5% and the bottom set of curves have a noise level of 1%. Left: Square pad pattern. Right: Sinusoidal pad pattern.

net gain over a simple square pattern in channel count. A scale factor of $L > 1$ corresponds to a reduction in channel count. Fig. 6 shows the median, 10th, and 90th percentile of the 2D position resolution function as L is varied for square pads (Left) and sinusoidal pads (Right).

While the two pad patterns have comparable resolutions at L close to 1, the sinusoidal pattern outperforms the square pattern out to $L = 2$. The divergence of the resolution in the square pattern at large L comes

from the image being fully contained within single pads with no sharing to constrain the position.

5. Distributed pads using pickup internal layers

There are applications that require large-area photo-coverage but have low occupancies, and for which time resolutions less than 100 psec are adequate [41]. These applications are natural for RF strip-line

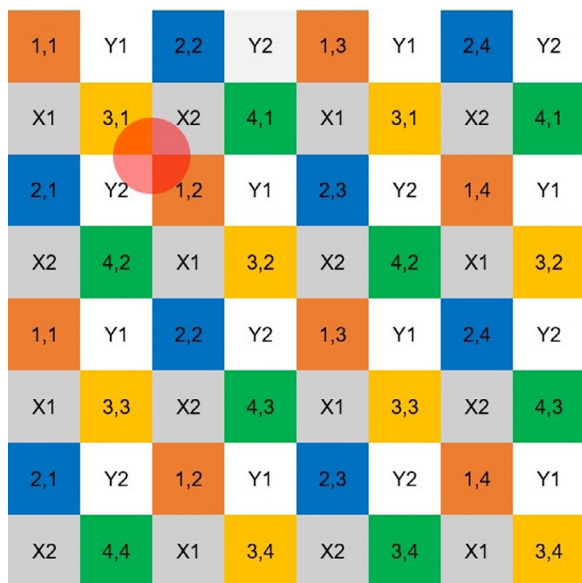


Fig. 7. An implementation of distributed pads on the pickup board. Half of the cells each have 2 indices, with the first index also represented by the color of the cell. Cells with the same two indices are connected together using internal layers on the printed circuit board. The other half are each connected to one of the four channels, X1, X2, Y1, Y2. In total, there are 20 distinct channels in this pattern. The size of the anode charge pattern is indicated by the disk in the upper left quadrant, corresponding to a scale factor of $L = 1.0$. (For interpretation of the references to color in this figure legend, the reader is referred to the web version of this article.)

readouts [6,33,42], which are 1-dimensional and for which the channel count scales linearly with area rather than quadratically.

However, the signal pickup board can be economically and quickly implemented as a multi-layer printed-circuit (PC) card, allowing multiple internal signal and ground layers to connect physically non-adjacent pads to produce a single electrical pad through vias and internal traces. These distributed pads can connect through vias and traces to front-end digitization electronics directly on the back of the signal card. Values of the scale factor L substantially less than 1.0 can also be explored.

The advantages for high-rate low-occupancy applications will depend on the individual application. Disadvantages include RF impedance mismatches, higher capacitance, and higher cross-talk. However the distributed pad solution may reduce the channel count for applications with a small charge image or requiring custom pad shapes.

Fig. 7 shows an example implementation (the ‘Park’ grid). Half of the cells each have 2 indices, with the first index also represented by the color of the cell. Cells with the same two indices are connected together using internal layers on the printed circuit board. The other half are each connected to one of the four channels, X1, X2, Y1, Y2. There are 64 pads total in this 8-by-8 array of cells. The first indices repeat with a period of 4 pads both vertically and horizontally. In odd-numbered columns, the second index remains constant across the whole column. In even-numbered rows, the second index remains the same. The channels X1, X2, Y1, and Y2 appear with a period of 4 pads both vertically and horizontally.

This pattern has a different scaling of channel count to digitized area, with an 8×8 array corresponding to 20 channels, a 16×16 array corresponding to 36 channels, and a 32×32 array corresponding to 68 channels. In general, a $4n \times 4n$ array has $8n + 4$ channels.

6. Summary

The development of large-area MCP-PMT photodetectors has opened the possibility of applications with photocoverage measured

in tens or hundreds of square meters with sub-millimeter spatial resolutions and time resolutions measured in tens of picoseconds. For high-rate applications, such as medical imaging and high-energy particle colliders, a highly-segmented readout is required. Thus an anode geometry consisting of pads is preferred over a strip geometry with a lower channel count. Incorporating a capacitively-coupled anode in the MCP-PMT allows complex patterns of pads to be easily implemented on a printed circuit card external to the vacuum package.

In a geometry consisting of an array of pads, the number of electronics channels is proportional to the area covered. We present here an example of the use of charge sharing among pads to lower the channel count per unit area while maintaining position resolution. The results from simulations are presented with the pad size scaled to the charge image at the anode, with signal intensities corresponding to the case of a single photoelectron or many photoelectrons induced by a charged particle. The simulated signal is represented as a signal image with intensity that varies as a bivariate Gaussian centered on the incident particle position. The signal sharing is calculated using the magnitude of overlap of this image with the pads.

The signal sharing can be enhanced by distorting pad patterns with convex/concave boundaries. A conventional pattern of regular square pads serves as the baseline for comparison of spatial resolution and channel count per unit area. The patterns are scaled to the diameter of the charge image, with a scaling factor L defined as the ratio of the pad pitch to the 4σ diameter of the Gaussian signal image. A value of L greater than 1.0 indicates a larger pad, and hence a lower channel count per unit area.

Noise from digitizing electronics, taken here from measured values as 7.5% and 1% of the total signal intensity induced by the charge cloud, increases the amount of overlap with neighboring pads required for a given spatial resolution.

As an example we present the simulation of a pattern with pad boundaries formed by horizontal and vertical sine functions. At a scaling factor of $L = 1.0$ the pattern returns a maximum spatial resolution for incident single photons of ≈ 800 microns over the full area, similar to that of the baseline square pad pattern. However, the sine pattern performs better as L increases. The pattern performs at $L = 1.5$ still with a maximum of $800 \mu\text{m}$, while the resolution of the square pattern diverges past $1000 \mu\text{m}$ for $L > 1.5$. The sine pattern allows a reduction in channel count by a factor of 2.25 with a typical resolution of ≈ 600 microns.

Capacitive coupling of the monolithic internal anode to the pattern of electrodes on an external signal pickup board allows the use of inexpensive, widely-available, and fast turn-around printed-circuit technology. For low occupancy applications, multi-layer printed circuit boards allow connecting non-adjacent pads in patterns that uniquely encode the position of the charge pattern. The encoded multi-layer pickup has the property that the number of channels scales linearly in the number of pads per linear length rather than quadratically as in the adjacent-pad case.

CRediT authorship contribution statement

Jinseo Park: Conceptualization, Methodology, Software, Validation, Formal analysis, Data curation, Writing - original draft, Writing - review & editing, Visualization. **Fangjian Wu:** Conceptualization, Methodology, Software, Validation, Formal analysis, Investigation, Data curation, Writing - original draft, Writing - review & editing, Visualization. **Evan Angelico:** Conceptualization, Methodology, Data curation, Writing - original draft, Writing - review & editing, Supervision. **Henry J. Frisch:** Conceptualization, Ideas, Resources, Writing - review & editing, Supervision. **Eric Spieglan:** Conceptualization.

Declaration of competing interest

The authors declare the following financial interests/personal relationships which may be considered as potential competing interests: Authors Angelico, Spieglan, and Frisch are Inventors of intellectual property on LAPPD technology held or applied for through the University of Chicago.

Acknowledgments

This work was supported by the High Energy Division of the Department of Energy, United States of America through awards DE-SC-0008172 and DE-SC-0020078. E. Angelico gratefully acknowledges funding by the DOE Office of Graduate Student Research (SCGSR) program, United States of America, managed by ORAU under contract number DE-SC0014664. All opinions expressed in this paper are the authors' and do not necessarily reflect the policies and view of DOE, ORAU, or ORISE. J. Park and F. Wu thank the Physical Sciences Division, Enrico Fermi Institute (EFI), and the College of the University of Chicago. We thank Mary Heintz of the EFI for superlative computing and electronics support.

Appendix. Calculating the signal distribution gradient

A discrete look-up table of signal distributions is used for calculating the signal-spatial gradient at each location on the anode pattern. We denote (x, y) as the position of the center of the charge cloud, or particle position, induced by the Cherenkov photons. The fraction of total signal that is measured on the i th pad is denoted as P_i , and is calculated based on the shape of the pad and the particle position:

$$P_i = P_i(x, y) \quad (1)$$

The signals induced by particles with positions x_j and y_k are numerically simulated and stored as a look-up table. The entries in the look-up table that represent the charge collected by pad i at each position (x_j, y_k) are defined as $T_i(x_j, y_k)$.

In a real (i.e. not simulated) detection event, the charge shower may land at location (x, y) which is close to but not exactly at a simulated point in the look-up table, (x_j, y_k) . If the two points are close enough, the following holds by linear approximation:

$$P_i(x, y) = T_i(x_j, y_k) + \frac{\partial}{\partial x} T_i(x_j, y_k)(x - x_j) + \frac{\partial}{\partial y} T_i(x_j, y_k)(y - y_k) \quad (2)$$

Considering the equation above for all pads, we define the following matrix form:

$$\begin{bmatrix} \dots \\ P_i(x, y) - T_i(x_j, y_k) \\ \dots \end{bmatrix} = \begin{bmatrix} \dots & \dots \\ \frac{\partial}{\partial x} T_i(x_j, y_k) & \frac{\partial}{\partial y} T_i(x_j, y_k) \\ \dots & \dots \end{bmatrix} \begin{bmatrix} x - x_j \\ y - y_k \end{bmatrix} \quad (3)$$

$$\Delta \mathbf{P} = \mathbf{J} \Delta \vec{r} \quad (4)$$

Since we want to calculate $\Delta \vec{r}$ from $\Delta \mathbf{P}$, we want a matrix \mathbf{K} such that

$$\mathbf{K} \mathbf{J} = \begin{bmatrix} 1 & 0 \\ 0 & 1 \end{bmatrix}$$

which implies

$$\Delta \vec{r} = \mathbf{K} \Delta \mathbf{P}. \quad (5)$$

Define

$$\partial_x \vec{T} = \begin{bmatrix} \dots \\ \frac{\partial}{\partial x} T_i(x_j, y_k) \\ \dots \end{bmatrix}, \partial_y \vec{T} = \begin{bmatrix} \dots \\ \frac{\partial}{\partial y} T_i(x_j, y_k) \\ \dots \end{bmatrix}$$

If $T_i(x_j, y_k)$ is defined as $T_{i,j,k}$ for short, $\partial_x \vec{T}$ and $\partial_y \vec{T}$ at each point could be calculated discretely:

$$\frac{\partial}{\partial x} T_i(x_j, y_k) \simeq \frac{T_{i,j+1,k} - T_{i,j,k}}{x_{j+1} - x_j} \quad (6)$$

$$\frac{\partial}{\partial y} T_i(x_j, y_k) \simeq \frac{T_{i,j,k+1} - T_{i,j,k}}{y_{k+1} - y_k} \quad (7)$$

We rewrite \mathbf{J} using $\partial_x \vec{T}$ and $\partial_y \vec{T}$:

$$\mathbf{J} = \begin{bmatrix} \partial_x \vec{T} & \partial_y \vec{T} \end{bmatrix}$$

\mathbf{K} may be calculated from the formula for the matrix inverse, only when $\partial_x \vec{T}$ is not parallel with $\partial_y \vec{T}$:

$$\mathbf{K} = \frac{1}{(\partial_x \vec{T})^2 (\partial_y \vec{T})^2 - (\partial_x \vec{T} \cdot \partial_y \vec{T})^2} \begin{bmatrix} (\partial_y \vec{T})^2 & -\partial_x \vec{T} \cdot \partial_y \vec{T} \\ -\partial_x \vec{T} \cdot \partial_y \vec{T} & (\partial_x \vec{T})^2 \end{bmatrix} \mathbf{J}^T \quad (8)$$

Given a set of signals \vec{P} collected by the pads in a measured charged-particle event, called the ‘‘signal distribution’’, one may find the particle position in a simulated look-up table that produces the smallest deviation from the observed signal distribution. If the signal collected by the i th pad from a particle impinging on position (x_j, y_k) is denoted in the look-up table \vec{T} as $T_i(x_j, y_k)$, then the reconstructed position of the particle \vec{r} is estimated by interpolating the deviation from the best-fit location (x_j, y_k) using the inverse-gradient matrix, \mathbf{K} , from above:

$$\vec{r} = \begin{bmatrix} x_j \\ y_k \end{bmatrix} + \mathbf{K}(x_j, y_k)(\vec{P}(x, y) - \vec{T}(x_j, y_k)) \quad (9)$$

The matrix \mathbf{K} depends on the geometry of the pad pattern used. It diverges at positions where $\partial_x \vec{T}$ is parallel with $\partial_y \vec{T}$, i.e. when a variation of the photon positions causes no change in the measured signal on the pads. In this case, the position resolution at that point is considered to be infinite and the pattern is dubbed ‘degenerate’.

When the anode pattern is not degenerate, the uncertainty of the measurement of the signal distribution, \vec{P} , results in an uncertainty in the reconstructed position, \vec{r} . Even if the look-up table were infinitesimally discretized and the shape of the charge-shower were perfectly known, \vec{r} would have some uncertainty cause by voltage noise of the digitizing electronics. The noise is characterized by a fractional RMS of σ_C at the percent level. The position uncertainties in x and y on \vec{r} , σ_x and σ_y , are then related to the charge noise by

$$\sigma_x^2 = \sum_{i=1}^{\# \text{ of pads}} (K_{0i}(x_j, y_k))^2 \sigma_C^2 \quad (10)$$

$$\sigma_y^2 = \sum_{i=1}^{\# \text{ of pads}} (K_{1i}(x_j, y_k))^2 \sigma_C^2 \quad (11)$$

The quantities in the main text that refer to position resolution are $\sigma = \sqrt{\sigma_x^2 + \sigma_y^2}$. The noise σ_C may be factored out so that the resolution functions reported may be scaled to be useful for other experimental setups with other noise factors.

References

- [1] M.J. Minot, et al., Large area picosecond photodetector (LAPPD™) offers fast timing for nuclear physics and medical imaging, *Il Nuovo Cimento C* 43 (2020).
- [2] B. Adams, et al., A brief technical history of the large-area picosecond photodetector (LAPPD) collaboration, 2020, Available at <https://arxiv.org/abs/1603.01843>. (Accessed 22 August 2020).
- [3] K. Inami, N. Kishimoto, Y. Enari, M. Nagamine, T. Ohshima, A 5 ps TOF-counter with an MCP-PMT, *Nucl. Instrum. Methods Phys. Res. A* 560 (2006) 303–308.
- [4] A. Ronzhin, M.G. Albrow, M. Demarteau, S. Los, S. Malik, A. Pronko, E. Ramberg, A. Zatserklyaniy, Development of a 10 ps level time of flight system in the Fermilab Test beam facility, *Nucl. Instrum. Methods Phys. Res. A* 623 (2010) 931–941.
- [5] J. Va'vra, D.W.G.S. Leith, B. Ratcliff, E. Ramberg, M. Albrow, A. Ronzhin, C. Ertley, T. Natoli, E. May, K. Byrum, Beam test of a time-of-flight detector prototype, *Nucl. Instrum. Methods Phys. Res. A* 606 (2009) 404–410.
- [6] B.W. Adams, A. Elagin, H. Frisch, R. Obaid, E. Oberla, A. Vostrikov, R. Wagner, J. Wang, M. Wetstein, Timing characteristics of large area picosecond photodetectors, *Nucl. Instrum. Methods Phys. Res. A* 795 (2015) 1–11.
- [7] E. Oberla, H.J. Frisch, Charged particle tracking in a water cherenkov optical time-projection chamber, *Nucl. Instrum. Methods Phys. Res. A* 814 (2016) 19–32.
- [8] E. Oberla, Charged particle tracking in a water cherenkov optical time projection chamber, 2020, Available at <https://search-proquest-com.proxy.uchicago.edu/docview/1732684282?accountid=14657>. (Accessed 22 August 2020).

- [9] F. An, et al., Neutrino physics with JUNO, *J. Phys. G* 43 (2016) 030401.
- [10] M. Askins, et al., THEIA: an advanced optical neutrino detector, *Eur. Phys. J. C* 80 (2020) 416.
- [11] H. Kim, H.J. Frisch, C.-M. Kao, Q. Xie, C.-T. Chen, L. Zhou, F. Tang, W.W. Moses, W.S. Choong, A multi-threshold sampling method for TOF PET signal processing, *Nucl. Instrum. Methods Phys. Res. A* 602 (2009) 618–621.
- [12] H. Kim, H.J. Frisch, C.-T. Chen, J.-F. Genat, F. Tang, W.W. Moses, W.S. Choong, C.-M. Kao, A design of a PET detector using micro-channel plate photomultipliers with transmission-line readout, *Nucl. Instrum. Methods Phys. Res. A* 622 (2010) 628–636.
- [13] H. Kim, H.J. Frisch, C.-T. Chen, J.-F. Genat, F. Tang, W.W. Moses, W.S. Choong, C.-M. Kao, A prototype TOF PET detector module using a micro-channel plate photomultiplier tube with waveform sampling, *Nucl. Instrum. Methods Phys. Res. A* 662 (2012) 26–32.
- [14] H.J. Frisch, E.J. Oberla, H.-J. Kim, M. Yeh, Positron-emission tomography detector systems based on low-density liquid scintillators and precise time-resolving photodetectors, 2016, US20180038968A1.
- [15] O. Jagutzki, A. Czasch, (RoentDek handels GmbH), ep3029490a1, 2015.
- [16] O. Jagutzki, A. Ceraso, A. Czasch, R. Dorner, M. Hattas, M. Huang, V. Mergel, U. Spillmann, K. Ullmann-Pfleger, T. Weber, H. Schmidt-Boecking, G.D.W. Smith, Multiple hit readout of a microchannel plate detector with a three-layer delay-line anode, *IEEE Trans. Nucl. Sci.* 49 (2002) 2477–2483.
- [17] O. Jagutzki, J. Barnstedt, U. Spillmann, L. Spielberger, V. Mergel, K. Ullmann-Pfleger, M. Grewing, H.W. Schmidt-Boecking, Fast-position and time-sensitive readout of image intensifiers for single-photon detection, in: *Proc. SPIE'S International Symposium on Optical Science, Engineering, and Instrumentation*, Vol. 3764, Denver, CO, United States, SPIE, 1999.
- [18] O. Jagutzki, A. Ceraso, A. Czasch, R. Dorner, M. Hattas, M. Huang, V. Mergel, U. Spillmann, K. Ullmann-Pfleger, T. Weber, H. Schmidt-Boecking, G.D.W. Smith, Multiple hit readout of a microchannel plate detector with a three-layer delay-line anode, *IEEE Trans. Nucl. Sci.* 49 (2002) 2477–2483.
- [19] J.S. Lapington, J.R. Howorth, J.S. Milnes, A reconfigurable image tube using an external electronic image readout, in: *Proc. Optics and Photonics 2005*, Vol. 5881, San Diego, California, United States, SPIE, 2005.
- [20] J.S. Lapington, J.R. Howorth, J.S. Milnes, Demountable readout technologies for optical image intensifiers, *Nucl. Instrum. Methods Phys. Res. A* 573 (2007) 243–246.
- [21] O. Jagutzki, A. Czasch, S. Schössler, Performance of a compact position-sensitive photon counting detector with image charge coupling to an air-side anode, in: *Proc. SPIE Defense, Security, and Sensing*, Vol. 8727, Baltimore, Maryland, United States, SPIE, 2013.
- [22] L.C. Garcia, Study of a prototype module of a precision time-of-flight detector for particle identification at low momentum, 2020, Available at <http://infoscience.epfl.ch/record/218636>. (Accessed 22 August 2020).
- [23] T. Conneely, et al., The TORCH PMT: a close packing, multi-anode, long life MCP-pmt for cherenkov applications, *J. Instrum.* 10 (2015) C05003.
- [24] Arradance Inc. has pioneered resistive coatings for micro-channel plates, 2020, Available at <https://www.arradance.com/>. (Accessed 22 August 2020).
- [25] J.W. Elam, A.U. Mane, J.A. Libera, J.N. Hryn, O.H.W. Siegmund, J. McPhate, M.J. Wetstein, A. Elagin, M.J. Minot, A. O'Mahony, R.G. Wagner, W.M. Tong, A.D. Brodie, M.A. McCord, C.F. Bevis, Synthesis, characterization, and application of tunable resistance coatings prepared by atomic layer deposition, *ECS Trans.* 58 (2013) 249–261.
- [26] A.U. Mane, W.M. Tong, A.D. Brodie, M.A. McCord, J.W. Elam, Atomic layer deposition of nanostructured tunable resistance coatings: Growth, characterization, and electrical properties, *ECS Trans.* 64 (2014) 3–14.
- [27] J.W. Elam, A.U. Mane, (Argonne national lab. (ANL), United States), tunable resistance coatings, 2013, US 20130335190A1.
- [28] Z. Insepov, V. Ivanov, S.J. Jokela, I.V. Vervovkin, A.V. Zinovev, Comparison of secondary electron emission simulation to experiment, *Nucl. Instrum. Methods Phys. Res. A* 639 (2011) 155–157.
- [29] E. Angelico, T. Seiss, B.W. Adams, A. Elagin, H. Frisch, E. Oberla, E. Spiegler, Capacitively coupled pickup in MCP-based photodetectors using a conductive metallic anode, *Nucl. Instrum. Methods Phys. Res. A* 846 (2017) 75–80.
- [30] F. Sauli, The gas electron multiplier (GEM): Operating principles and applications, *Nucl. Instrum. Methods Phys. Res. A* 805 (2016) 2–24.
- [31] A. Bressan, R. De Oliveira, A. Gandi, J.-C. Labbé, L. Ropelewski, F. Sauli, D. Mörmann, T. Müller, H.J. Simonis, Two-dimensional readout of GEM detectors, *Nucl. Instrum. Methods Phys. Res. A* 425 (1999) 254–261.
- [32] T. Credo, H. Frisch, H. Sanders, R. Schroll, F. Tang, Picosecond time-of-flight measurement for colliders using Cherenkov light, in: *Proc. IEEE Nuclear Science Symposium Conference*, Rome, Italy, 2004.
- [33] E. Angelico, Development of large-area MCP-PMT photodetectors for a precision time-of-flight system at the fermilab test beam facility, 2020, Available at <https://doi.org/10.2172/1637600>. (Accessed 22 August 2020).
- [34] M. Saito, Y. Saito, K. Asamura, Spatial charge cloud size of microchannel plates, *Rev. Sci. Instrum.* 78 (2007) 023302.
- [35] J.L. Wiza, Microchannel plate detectors, *Nucl. Instrum. Methods* 162 (1979) 587–601.
- [36] A.S. Tremsin, O.H.W. Siegmund, Spatial distribution of electron cloud footprints from microchannel plates: Measurements and modeling, *Rev. Sci. Instrum.* 70 (1999) 3282.
- [37] J.V. Jelley, Čerenkov Radiation, and its Applications, Pergamon Press, New York, 1958.
- [38] Schott borofloat 33, Brochure of optical, chemical, and thermal properties, 2020, Available at https://psec.uchicago.edu/glass/borofloat_33_e.pdf. (Accessed 22 August 2020).
- [39] Schott, glass made of ideas, 2020, Available at <https://www.schott.com/english/index.html>. (Accessed 22 August 2020).
- [40] E. Oberla, J.-F. Genat, H. Grabas, H. Frisch, K. Nishimura, G. Varner, A 15 GSa/s, 1.5 GHz bandwidth waveform digitizing ASIC, *Nucl. Instrum. Methods Phys. Res. A* 735 (2014) 452–461.
- [41] A. Elagin, R. Jiang, Space-time discriminant to separate double-beta decay from 8B solar neutrinos in liquid scintillator, 2019, Available at <https://arxiv.org/abs/1902.06912>. (Accessed 22 August 2020).
- [42] F. Tang, C. Ertley, J.-F. Genat, J. Anderson, K. Byrum, G. Drake, E. May, G. Sellberg, Transmission-line readout with good time and space resolutions for planacon MCP-PMTs, in: *Proc. Topical Workshop on Electronics for Particle Physics*, Naxos, Greece, 2008, CERN-2008-008.